Soft Matter

PAPER

Check for updates

Adhesion-based sorting of blood cells: an adhesive dynamics simulation study†

Anil K. Dasanna 🆔 and Ulrich S. Schwarz 🆔 *

Blood cells can be sorted in microfluidic devices not only based on their sizes and deformability, but also based on their adhesive properties. In particular, white blood cells have been shown to be sorted out by using adhesive micropatterns made from stripes that are tilted in regard to the direction of shear flow. Here we use adhesive dynamics simulations for round cells to quantitatively investigate this effect and to predict the optimal tilt angle. We then apply our method to predict optimal sorting conditions for malaria-infected red blood cells, which like white blood cells also adhere to and roll on adhesive substrates.

1 Introduction

Sorting different cell types or separating a cell type of interest from a heterogeneous population is of large importance for biological research and medical diagnostics.[1–3] In an active approach like the widely used method of fluorescent activated cell sorting (FACS) or magnetic activated cell sorting (MACS), labels are used to decide which cells have to be subjected to a sorting force. Much effort has been devoted also to develop passive approaches, that do not require any label and can work with smaller devices. Physical properties that are typically used in this context are cell size, shape, density, polarizability and deformability. In pinched flow fractionation, particles with varying sizes are separated by creating spreading flow profiles using repeated constrictions in a microchannel.[4–6] Deterministic lateral displacement devices use arrays of obstacles to bifurcate the trajectories of different cell types.[7–11] Real-time deformability cytometry monitor cell deformations in small constrictions with a fast camera.[12,13]

Passive approaches for cell sorting exploit the fact that physical differences between the different cell types lead to differential interactions with hydrodynamic flow in structured environments. Interestingly, a same reasoning can be applied also to adhesive interactions under flow. The paradigmatic case of an adhesively interacting blood cell is the leukocyte, that in combination with shear flow leads to the phenomenon of rolling adhesion.[14,15] Rolling adhesion is the intermediate step of the extravasation cascade that leukocytes use to exit the blood stream in response to inflammation or injury in the

surrounding tissue. The key receptor on leukocytes for rolling adhesion is P-selectin glycoprotein ligand-1 (PSGL-1) interacting mainly with P-selectin on the vascular endothelium. By micropatterning P-selectin in adhesive stripes that are titled in respect to the direction of flow (as shown schematically in Fig. 1), it has been shown that leukemic myeloid HL60 cells can be separated from other cells such as RBCs.[16–18]

Applications for cell sorting devises not only include the detection of circulating tumor or stem cells, but also the detection of parasites in the blood.[19] For example, deterministic lateral displacement devices have been used to sort out trypanosomes, the causative agents of the sleeping disease.[20] Another very
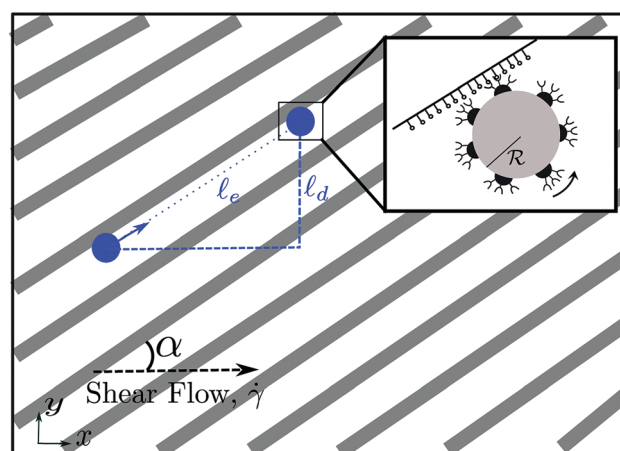

Fig. 1 Schematic diagram of a cell of radius R rolling in shear flow of shear rate $\dot{\gamma}$ over an adhesive micropattern. The receptors on the cell surface establish bonds with the ligands on the substrate that are arranged in stripes making an angle α with the shear flow direction. The total distance travelled along the stripe edge is ℓ_e and the lateral displacement is $\ell_d = \ell_e \sin \alpha$.

BioQuant and Institute of Theoretical Physics, Heidelberg University, Heidelberg, Germany. E-mail: schwarz@thphys.uni-heidelberg.de

important application in parasitology is to sort malaria-infected red blood cells (iRBCs) out of the blood of infected patients. iRBCs are known to have decreased deformability compared to wildtype RBCs.[21] It has been shown that they can be separated using *e.g.* margination in thin capillaries[22] or non-inertial lift forces.[23] Very recently, iRBCs have also been detected using real-time deformability cytometry.[24] Here we suggest that iRBCs can also be sorted based on their cytoadhesive properties, because iRBCs not only become less deformable, but also strongly adhesive upon malaria infection.

Malaria is an infectious disease that in humans is caused mainly by the eukaryotic parasite *Plasmodium falciparum* which is transmitted into the skin of the host during a mosquito blood meal.[25] Clinical symptoms of malaria appear when the parasites start to invade RBCs. The infectious cycle inside an iRBC takes 48 hours until rupture and release of around 20 new parasites. In order to avoid clearance by the spleen of the stiffened iRBC, the parasite induces adhesive knobs on the iRBC-surface. Like for leukocytes, this leads to rolling adhesion on the vascular endothelium and thus to longer residence times in the vasculature. Adhesiveness is provided by the localization of the parasite protein Plasmodium falciparum Erythrocyte Membrane Protein-1 (PfEMP-1) to the knobs, which binds endothelial factors such as ICAM-1, CD36 or CSA. In fact it has been noted before that the design of the adhesive structure of the iRBC is very similar to the one of leukocytes: both present their adhesion molecules in clusters on elevated platforms on the cell surface, namely microvilli for leukocytes and knobs for iRBCs.[26] Thus one might expect that iRBCs can be sorted out of blood through their adhesive interactions in a similar manner as leukocytes. However, a quantitative understanding of such processes is missing and a possible design for such a device has not been described yet.

Here we address sorting of blood cells on micropatterned adhesive stripes using adhesive dynamics simulations. Adhesive dynamics has been initially introduced to quantitatively describe the interplay between hydrodynamic flow of spherical particles above a wall and receptor–ligand bond dynamics in the contact zone.[27,28] Later this model was extended by including spatial resolution to both receptors and ligands[29–32] and deformability.[33,34] Adhesive dynamics with spherical particles is usually applied to leukocytes, but recently has been applied also to late-stage iRBCs, which in contrast to early-stage iRBCs are round.[35] For early-stage iRBCs, one has to implement adhesive dynamics for non-spherical particles, typically using mesoscopic simulation methods for the hydrodynamic part, such as dissipative particle dynamics.[36,37] The multiscale approach provided by adhesive dynamics has shown that depending on the microscopic model parameters, different dynamic states emerge at the cell scale, like firm adhesion, rolling adhesion, transient adhesion and free flow.

In order to explore the potential of sorting adhesive cells in hydrodynamic flow, here we use adhesive dynamics simulations of spherical particles in the rolling adhesion regime and simulate their flow over an array of tilted adhesive stripes. In contrast to computationally expensive models for non-spherical

or deformable cells, this approach allows us to accumulate very good statistics. We will first characterize the resulting motion and compare to experimental results of sorting HL60-cells in shear flow using asymmetric P-selectin patterns. We will then show that this approach can be extended to sort or separate iRBCs with different levels of adhesiveness. By considering known cell features such as iRBC knob densities, we will propose experimentally relevant parameters such as shear rate and angle of inclination which should lead to successful sorting.

2 Model

The dynamics of a spherical cell of radius R in shear flow of velocity $u^\infty = \dot{\gamma}z\mathbf{e}_x$ is simulated using the following Langevin equation:[30,38]

$$\partial_t X(t) = u^\infty + M\{\mathbf{F}_D + \mathbf{F}_S\} + k_B T\nabla M + \xi(t) \qquad (1)$$

where $X(t)$ is a six-dimensional vector representing both position and orientation, and M is the mobility matrix which depends on the position of the cell above a wall. The forces $\mathbf{F}_D$ and $\mathbf{F}_S$ are direct and shear forces, respectively. Direct forces arise from gravity and bond dynamics in the contact zone. The third term in eqn (1) is a spurious drift term which disappears when the mobility matrix is position-independent. The last term represents a stochastic random force which results from the thermal bath and obeys the fluctuation–dissipation theorem:

$$\langle \xi(t) \rangle = 0,$$

$$\langle \xi(t)\xi(t') \rangle = 2k_B TM\delta(t - t'). \qquad (2)$$

To make eqn (1) non-dimensional, we scale all the lengths by the radius R of the sphere, time by inverse shear rate, $1/\dot{\gamma}$, and forces by the Stokes force $6\pi\eta R^2\dot{\gamma}$ at velocity $R\dot{\gamma}$. We then numerically solve the discretized Langevin equation eqn (1):

$$X(\tau + \delta\tau) = X(\tau) + [u^\infty + M\{\mathbf{F}_D + \mathbf{F}_S\}]\delta\tau$$
$$+ \frac{1}{\text{Pe}}\nabla M\delta\tau + \sqrt{\frac{1}{\text{Pe}}}\mathbf{B} \cdot \tilde{\xi}(\tau) \qquad (3)$$

where the new dimensionless number in the above equation is the Peclet number $\text{Pe} = (6\pi\eta R^3\dot{\gamma})/(k_B T)$, which represents the importance of advection *versus* diffusion. The motion is deterministic for $\text{Pe} > 1$ and diffusive for $\text{Pe} < 1$. $\mathbf{B}$ follows from $M = \mathbf{B}\mathbf{B}^T$. In the last term $\tilde{\xi}(\tau)$ is a six-dimensional random vector generated using a Gaussian distribution with mean 0 and standard deviation 1. Updating the translational part of $X(\tau)$ is straightforward. To update the rotational part of $X(\tau)$, we use Rodrigues' formula:

$$\mathbf{n}_i' = \hat{\theta}(\hat{\theta}\cdot\mathbf{n}_i)(1 - \cos(\theta)) + \mathbf{n}_i\cos(\theta) + \hat{\theta} \times \mathbf{n}_i\sin(\theta) \qquad (4)$$

where $\mathbf{n}_i$ and $\mathbf{n}_i'$ are basis orthonormal vectors (which are fixed at the center of mass of the sphere) before and after rotational update, respectively. $\hat{\theta}$ is the unit rotation vector.

The ligands are arranged on the substrate in a simple cubic lattice within the adhesive regions of the stripe pattern

as shown in Fig. 1. Bond dynamics is employed at each time step between the receptors on the cell and the ligands on the substrate. For formation of the receptor–ligand bond, we use the concept of an encounter complex: when the distance between receptor and ligand is less than the encounter distance r_0, a bond can be formed with the constant on-rate κ_{on}. We use Bell's equation for bond dissociation: the off-rate depends exponentially on the tensile force from the receptor–ligand bond, $\kappa_{off} = \kappa_{off}^0 \exp(F/F_d)$, where κ_{off} is the unstressed off-rate and F_d is the internal force scale.[39] We model the mechanics of the receptor–ligand bond as a cable:[40]

$$\mathbf{F}(\mathbf{r}) = \kappa(\mathbf{r} - \mathbf{r}_0)\Theta(\mathbf{r} - \mathbf{r}_0) \qquad (5)$$

where Θ is the Heaviside step function, κ is the spring constant and $\mathbf{r}_0$ is the bond with length ℓ_0 at the time of bond formation. The probability for bond formation at given time step $\delta\tau$ is $p_{on} = 1 - \exp(-\kappa_{on}\delta\tau)$ and for bond dissociation it is $p_{off} = 1 - \exp(-\kappa_{off}\delta\tau)$.

We choose reasonable parameters for our purpose. Interestingly, they seem to be rather similar for leukocytes and iRBCs.[26] The radius of the spherical cell is chosen as $R = 4$ μm, which is close to both the radius of a leukocyte and the radius of a late-stage iRBC. The shear rate is chosen within the range of 30 Hz to 50 Hz, which is the typical range over which rolling adhesion occurs in capillaries and corresponding flow chamber experiments. Viscosity is chosen to be the typical one for an aqueous solution, $\eta = 1$ mPa s. For the receptor–ligand bond kinetics, the encounter length is chosen as $r_0 = 50$ nm. This choice is motivated by the observations that the typical linker length for the unstressed receptor–ligand bonds of leukocytes are few tens of nanometers[41] and that for iRBCs, the knob height is around 20 nm and the length of PfEMP1 molecule is close to 30 nm.[42,43] In adhesive dynamics, one usually chooses relatively generous values for the encounter length, to relax the strong assumptions of rigid spheres and no-slip boundary conditions. The force scale in Bell's equation is chosen as $F_d = 10$ pN, following standard choices in the literature.[30,31,35] For example, the force scale for the PSGL-1:P-selectin bond in leukocyte adhesion has been estimated to be around 10–50 pN,[44–47] which is close to the estimate 10 pN for the PfEMP-1:CD36 bond.[48] The spring constant is chosen to be 0.5 pN nm^{-1}.[35] While leukocytes adhere through molecular clusters at the tips of microvilli, iRBCs do so through adhesive clusters on knobs. In the following we therefore use adhesive patches to describe both cases. The density of microvilli in leukocytes is around 3–6 μm^{-2} [49–51] and the typical knob density for iRBCs is 5–10 μm^{-2},[52] so they both are very similar. Receptors are distributed over the adhesive patches with a Poisson distribution with a mean value of 6 (multiplicity).[35] The widths of the adhesive and non-adhesive stripes of the ligand pattern is 4 μm and 8 μm, respectively.[16] The ligand spacing within each adhesive stripe is 80 nm. As shown in Fig. 1, the stripe patterns makes a finite angle α with the shear flow direction, which is along the x-direction.

3 Results

3.1 Leukocyte rolling on a stripe substrate

We start by comparing our adhesive dynamics simulation results for sticky cells on adhesive stripe patterns with leukocyte rolling on biofunctionalized stripe patterns, for which experimental data are available. The interplay between the microscopic bond dynamics and the macroscopic determinants such as shear rate and viscosity leads to the emergence of dynamic states, namely firm adhesion, rolling adhesion, transient adhesion and free flow. We classify these dynamic states by considering average translational and rotational velocities.[30,35] For firm adhesion, both translational velocity v and rotational velocity Ω are close to zero, as the cell is firmly bound to one position. For free flow, they are close to their hydrodynamic values. Rolling is characterized by synchronization of the translational and rotational velocities, such that $R\langle\Omega\rangle/\langle v\rangle \geq 0.80$. All other states are classified as transient adhesion. Here we use on and off-rates such that the resulting dynamical state on the homogeneous substrate is always rolling adhesion. For a cell rolling along the flow direction for $\alpha = 0$, only the x-component of translational velocity and the y-component of the rotational velocity are non-zero. In our case, as the cell rolls along patterns with a small inclination α in respect to the flow direction, it has a finite y-component of translational velocity and (y,z)-components of angular velocity. Because these components are small, in the following we only show the components present at $\alpha = 0$.

In Fig. 2(A), we show five representative trajectories of a leukocyte rolling on ligand patterned substrate with inclination angle $\alpha = 6°$. Every trajectory consists of alternating periods of movement over non-adhesive and adhesive parts of the substrate. The second part is further subdivided into movement with the flow across the stripe and subsequent edge tracking with the given inclination angle, until the cell detaches. In Fig. 2(B), we show both translational and angular velocities of one of the representative trajectories over the stripe pattern. The peaks in the translational velocity correspond to the non-adhesive parts, where the cells moves close to the hydrodynamic velocity. We further note that the movement over the adhesive parts seems to accelerate. In Fig. 2(C), we zoom into the movement over a single stripe for large stripe width. This shows that the cell only accelerates once it reaches the edge of the stripe, as marked by an arrow, and then again once it starts to detach. Movement along the edge is presumably faster because contact area is reduced. We conclude that translational and angular velocities vary in an oscillatory fashion, reaching large (hydrodynamic) velocities over non-adhesive regions and smaller values when rolling on adhesive stripes. The rolling part in turn consists out of two parts: rolling in x-direction with the flow over the stripe, and then faster rolling along the edge with the given inclination angle α (compare ESI,† Movie S1).

A detailed analysis shows that the first part of the adhesive part is stable rolling, while the second part is transient adhesion, as one would find it on a homogeneous substrate for high shear rates and low ligand or receptor densities. This effect becomes stronger with increasing inclination angle. For example, for inclination
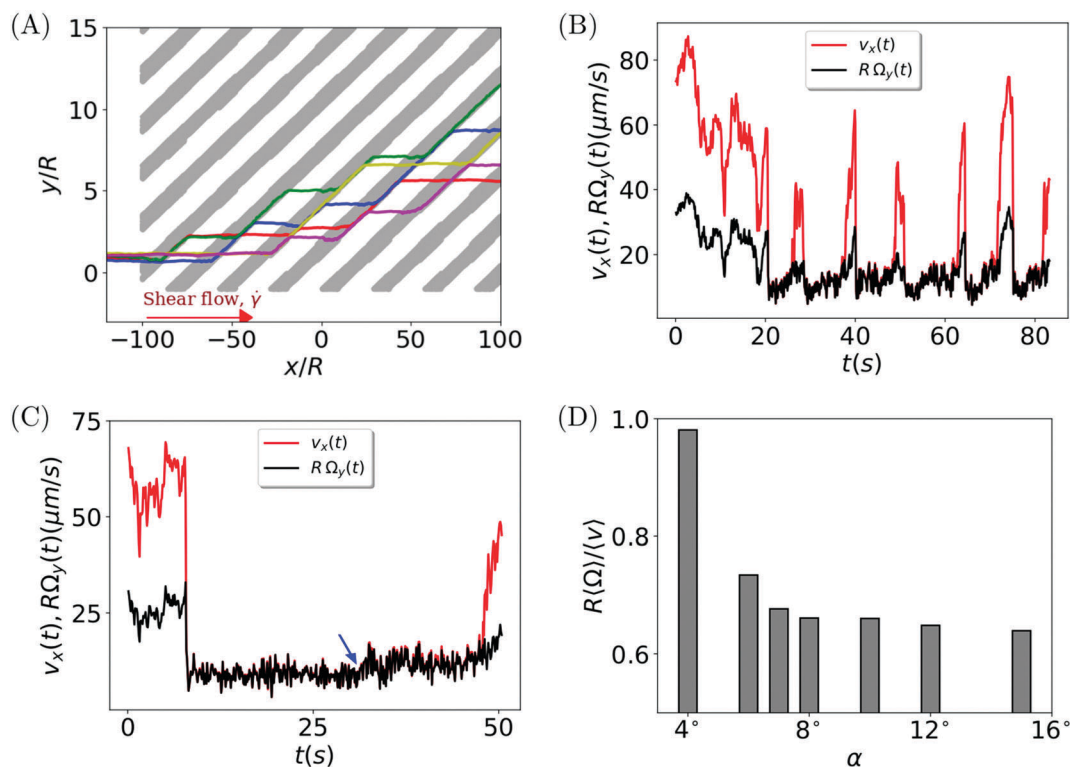
Fig. 2 (A) Five representative trajectories of a leukocyte rolling on ligand patterned substrate with inclination angle of $\alpha = 6°$. The shear flow is along x-direction and shear rate is 40 Hz. Translational velocity (x-component) and y-component of angular velocity of a representative cell over striped patterns (B) and over a single stripe (C) are shown. The arrow in (C) corresponds to the position of the edge, where the cell becomes faster. (D) Ratio of average angular to translational velocities is shown against inclination angle α.

angle $\alpha = 4°$, the synchronization ratio is $R\langle\Omega\rangle/\langle v\rangle \simeq 0.98$, and for inclination angle $\alpha = 6°$, the ratio is found to be 0.73. For even higher angles such as $\alpha = 10°$ or $\alpha = 15°$, the ratio approaches 0.63 as shown in Fig. 2(D). Note however that this value is still above the hydrodynamic value of 0.57 that one gets for slipping motion in shear flow close to a wall without adhesion.[30] Together, these results indicate an important limitation of the stripe sorting assays, namely that increasing inclination angles destabilizes the rolling motion. In addition, rolling adhesion is destabilized also by increased shear rate. While small inclination angles and low shear rates are favorable for stable rolling, they reduce the efficiency of the sorting devise. Therefore the question arises how optimal sorting can be achieved.

3.2 Lateral displacement

We next characterized lateral displacement in quantitative detail. The key parameters that characterize the leukocyte trajectories on stripe patterns are its mean edge tracking length $\langle\ell_e\rangle$ or mean lateral displacement $\langle\ell_d\rangle$ (compare Fig. 1), which strongly depend on edge inclination angle α and shear rate $\dot{\gamma}$. The track along the edge is extracted by fitting two straight lines to the two different parts of the trajectory over the adhesive stripe. As shown in Fig. 3(A) for $\alpha = 6°$, the distribution of the edge tracking lengths is found to follow an exponential distribution, $P(\ell_e) = e^{-\ell_e/\lambda}/\lambda$, where $\lambda = 106.56$ μm denotes the mean edge tracking length. This suggests that detachment

effectively is a Poisson process. The cumulative distribution function (CDF) of edge tracking length follows as $\text{CDF}(\ell_e) = 1 - e^{-\ell_e/\lambda}$. In Fig. 3(B), we show CDFs for different inclination angles, namely $\alpha = 6°$, $7°$, $8°$, $10°$. The agreement between the simulation results (symbols) and the exponential functions (lines) is very good. In Fig. 3(C), it is shown that the mean tracking length λ decreases exponentially with the edge inclination angle α. The data are fitted by the exponentially decreasing function, $\log(\lambda(\alpha)) = -0.95\alpha + 10$. In Fig. 3(D) we plot the lateral displacements against the edge inclination angle, which is expected to vary as $\langle\ell_d\rangle = \lambda(\alpha)\sin(\alpha)$ (dashed line), exactly as found from the simulations (symbols).

We next studied the effect of shear rate on edge tracking length and thereby lateral displacements. In Fig. 3(E), we show that the edge tracking length decreases as shear rate increases from 35 Hz to 50 Hz. The edge tracking length decreases from 286 μm to 40 μm, which corresponds to the lateral displacement decreasing from 30 μm to 4 μm. Sufficient amount of bond formation at the front is necessary to balance bond rupture under shear force and to keep the motion along the edge going. This is verified in the simulations by increasing on-rate and indeed one observes an increase in the tracking length if the on-rate is increased. Increasing on-rate or decreasing shear rate results in the same effect as the ratio $\kappa_{on}/\dot{\gamma}$ sets the dimensionless on-rate in the problem. Decreasing the effective on-rate $\kappa_{on}/\dot{\gamma}$ also increases rolling velocity along the edge. Rolling velocities along the edge are shown in Fig. 3(F)

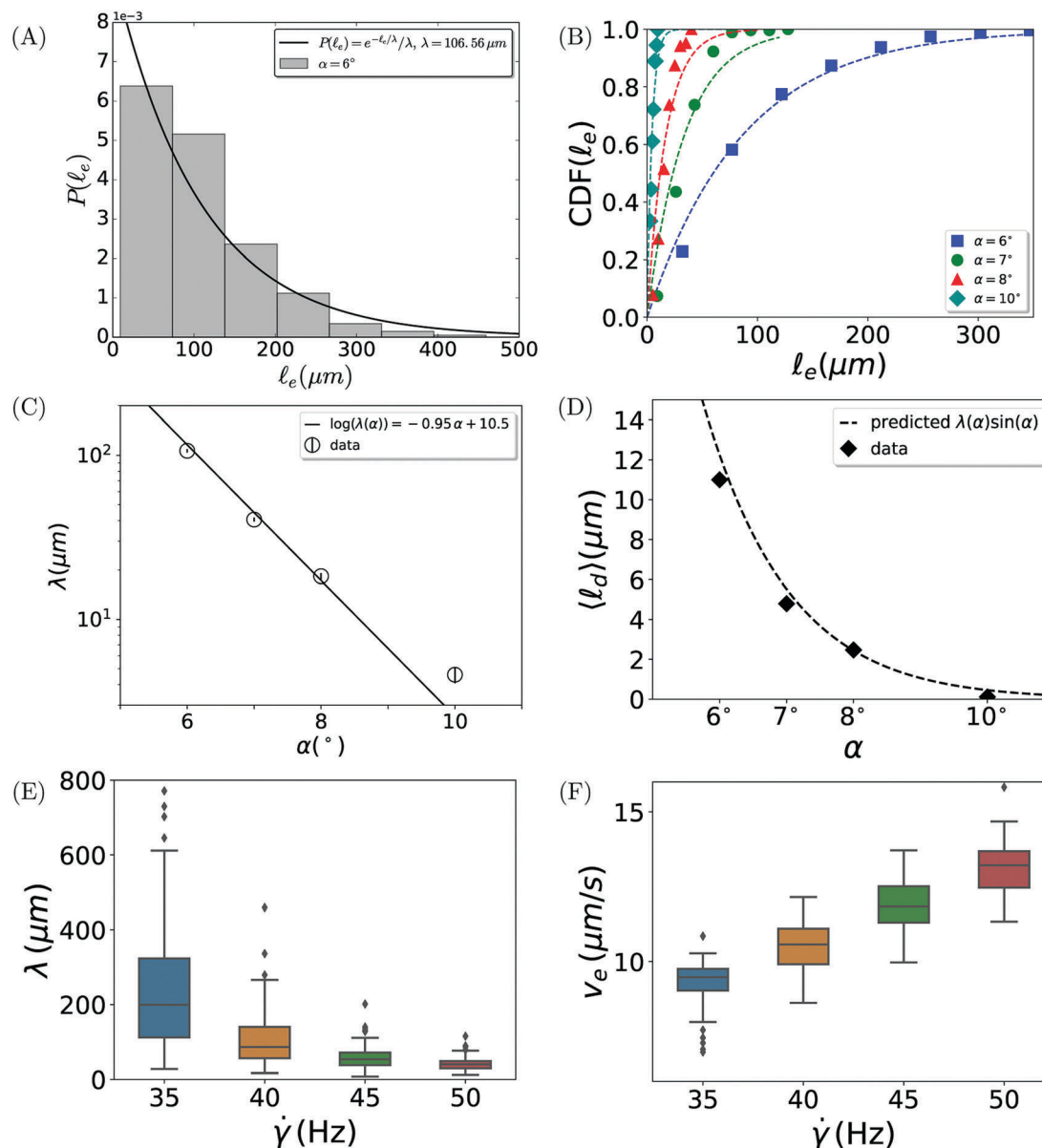**Fig. 3** (A) Edge tracking length distribution of leukocytes is plotted for shear rate $\dot{\gamma} = 40$ Hz and inclination angle $\alpha = 6°$. The knob density is 7.5 knobs per μm^2. The on and off rates are $\kappa_{on} = 40$ Hz and $\kappa_{off}^0 = 4$ Hz. The probability density is fitted well with an exponential distribution. (B) Cumulative distribution functions (CDFs) for four edge inclination angles. Simulations (symbols) and the exponential model (lines) agree very well. (C) Mean edge tracking lengths for different values of edge inclination angles are shown and the data is fitted with an exponentially decreasing function. (D) Mean lateral displacement *vs.* inclination angle is plotted along with the predicted lateral displacement from a Poisson process, $\langle \ell_d \rangle = \lambda(\alpha)\sin(\alpha)$ where $\lambda(\alpha)$ is the fitted function in (C). (E) Edge tracking lengths and (F) edge velocities for different shear rates are shown. The edge inclination angle is $\alpha = 6°$.

and range from $\nu_e = 10$ to 15 $\mu m\ s^{-1}$ when increasing shear rate from 35 Hz to 50 Hz.

In summary, our simulations give very similar results as the experiments for HL60 cells using P-selectin patterns.[16] The experimentally achieved total tracking lengths are prohibitively large for our computer simulations, but the functional dependencies are the same, suggesting that our model captures the main aspects. We note that very small angles are problematic, because there is no well-defined lateral displacement yet. Starting with $\alpha \approx 6°$, however, the sorting assay works as expected. In the simulations we observe that the edge tracking length diverges when the inclination angle is closer to zero, because the cell tends to move inside the stripe rather than at its edge, which is the essential sorting effect.

3.3 Optimal inclination angle

We next investigated the relationship between total lateral displacement and the edge inclination angle. We define the total lateral displacement as:

$$L_d = \sum_i \ell_d \approx n\lambda(\alpha)\sin(\alpha) \qquad (6)$$

where the summation runs over all the stripes in a grid and the approximation should become valid if the number n of stripes is large. We here assumed that cell binds to every stripe during its motion, which is a fair assumption for lower shear rate flows and for high ligand–receptor densities. Let the total dimension of the grid along x-direction be D and x_d the width of the non-adhesive part of the stripes, which is 8 µm in the current simulations. We also assume that the adhesive stripes are half as wide as the non-adhesive ones. For grids with a high number of stripes, the summation in eqn (6) can be approximated by a simple expression. To do this, we equate the total displacement of the cell along x-direction during edge tracks and non-edge tracks with the total x-dimension of the grid. When the cell is at the stripe edge, its displacement along x-direction has two contributions before reaching next stripe edge: (1) when the cell moves along the edge and (2) when it moves along non-edge track (which includes both non-adhesive and adhesive region before reaching the edge). When the cell detaches from edge, it has to cover $3x_d/(2\sin(\alpha))$ distance before it reaches the next consecutive edge and it covers an average distance of $\lambda(\alpha)\cos(\alpha)$ along the flow direction when it moves along the edge. So the number of edge tracks become

$$n \simeq \frac{D}{\left(\dfrac{3x_d}{2\sin(\alpha)} + \lambda(\alpha)\cos(\alpha)\right)}. \quad (7)$$

Thus, the total lateral displacement in eqn (6) becomes

$$L_d = \left(\frac{D}{\left(\dfrac{3x_d}{2\sin(\alpha)} + \lambda(\alpha)\cos(\alpha)\right)}\right)\lambda(\alpha)\sin(\alpha)$$

$$= \frac{2D\lambda(\alpha)\sin^2(\alpha)}{(3x_d + 2\lambda(\alpha)\sin(\alpha)\cos(\alpha))}. \quad (8)$$

For smaller angles, the edge tracking length becomes large enough to cover the full trajectory. This results in the simple expression for total lateral displacement of $L_d \simeq D\tan(\alpha)$. The two expressions for L_d are plotted in Fig. 4 along with the simulation data for leukocytes for different inclination angles. The agreement is reasonably good and one clearly sees the crossover between the two cases. The small angle approximation $D\tan(\alpha)$ is shown as a line and for the large angle approximation, we use $\lambda(\alpha)$ from above. Together our results show that for given bond kinetic parameters and grid dimensions, maximum total lateral displacement is achieved for an intermediate (optimal) angle rather than for higher or lower inclination angles. Though large lateral displacements can be achieved with large inclination angles, stripe patterns with large inclination angles has less tracking length and the dynamic state becomes very instable. Although grids with small inclination angles have large tracking lengths, this requires very large grids to achieve reasonably good lateral displacements. These two conditions limit the edge inclination angle to an optimal value for producing maximum total lateral displacement.
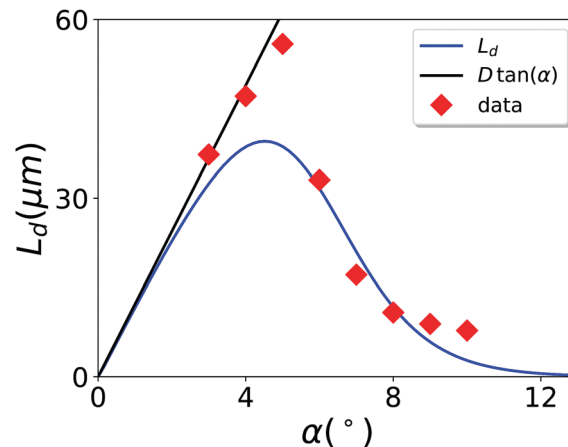

Fig. 4 Total lateral displacements of leukocytes for the grid shown in Fig. 2(A). The blue line is eqn (8) for L_d for many stripes and the black line is the linear approximation for one stripe. The simulated data (symbols) agree in the two limiting cases and have a maximum inbetween.

3.4 Adhesive footprint

Next we discuss the adhesive footprint of a cell rolling on a stripe pattern and how the edge inclination angle affects the footprint. Adhesive footprints are discussed by analyzing the positions of the patches at which new bonds form and old bonds break, with varying edge inclination angle. In Fig. 5(A)–(D), we show adhesive footprints of cell rolling on stripes of inclination angles $\alpha = 0°$, $\alpha = 6°$, $\alpha = 10°$ and $\alpha = 15°$, respectively. Black hexagons represent positions of the patches at which old bonds are broken and the density map shows the patch positions (projected on plane) at which new bonds form (for $\alpha = 15°$, supplemental movie S2 (ESI†) shows the positions where new bonds are formed in blue and old bonds are broken in orange, respectively). All patch positions are displayed with reference to the center of mass system. The shear rate, on-rate and off-rate are chosen to be 30 Hz, 30 Hz and 3 Hz. Our first observation is that the overall contact area is reduced when the edge inclination angle α is increased. The contact area is found to be 1.41 µm² for $\alpha = 0°$ and a smaller contact area of 1.15 µm² is found for $\alpha = 15°$. In a simplest case, when a sphere of radius R is in contact with the plane, the radius of contact zone, a, created at a depth of r_0 becomes $\approx \sqrt{2Rr_0}$. For an encounter radius of $r_0 = 50$ nm, the contact area becomes 0.63 µm², which is close to the values that we measured for the footprints.

The patches at which bonds break seem to be distributed all over the contact zone, though higher density of patches appear at the rear end. This distribution depends on the cell's velocity or dynamic state, such as rolling adhesion or transient adhesion. For a cell that is moving through transient adhesion, as it typically happens during edge tracking, old bonds mainly break at the rear end of the cell.[35] It is clear from the figure that the density of patches at which bonds form is higher at the front side of the cell, which is a characteristic feature of rolling adhesion. As the edge inclination angle increased, a higher density of patches at which new bonds are formed develops in the stripe direction. For example, for edge inclination angle
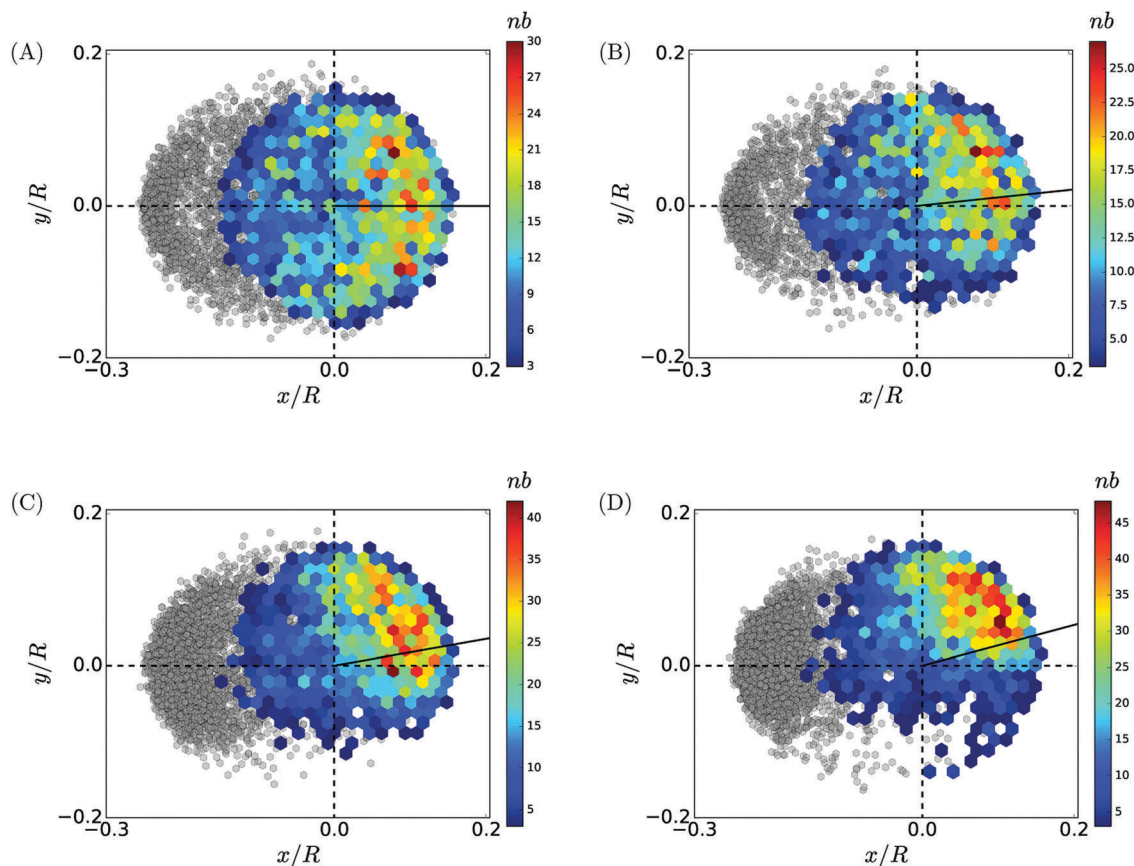
Fig. 5 Adhesive footprint of leukocytes rolling along the edge with an inclination angle (A) $\alpha = 0°$, (B) $\alpha = 6°$, (C) $\alpha = 10°$ and (D) $\alpha = 15°$. The gray and color hexagons represent x and y positions of patches for which bonds are broken and form, respectively. The color coding variable nb represents number of bonds formed. The positions of patches are displayed in the center of mass system of the cell.

$\alpha = 15°$, a high density area of patches completely shifted to top right quadrant as shown in Fig. 5(D). Along with this shift, patch positions at which old bonds break become asymmetric with increasing inclination angle. Both these observations signify the fact that increasing edge inclination angle decreases the contact area, which increases the cell velocity and changes rolling into transient adhesion.

3.5   Sorting of malaria-infected cells

We finally address sorting of malaria-infected red blood cells (iRBCs). Similar to microvilli in leukocytes, the iRBC develops adhesive knobs on its surface during parasite maturation. PfEMP-1 receptors, exported by the parasite into the cytosol, are anchored to the knobs. Knobs start appearing at the end of the first half of the 48 hours infectious cycle and their number gradually increases till the end of the cycle. Therefore they are an excellent feature to sort iRBC according to their progression through the cycle. We choose knobs densities of 5, 7.5 and 10 knobs per μm^2 for rings, trophozoite and schizont stage cells, respectively. For all three types of cells, we used the same stripe pattern with inclination angle of $\alpha = 8°$. The ligand density in the adhesive regions is taken to be 156 μm^{-2}, the same as for the leukocytes. The shear rate is chosen to be $\dot{\gamma} = 30$ Hz. We used off-rate of 0.77 Hz and force scale $F = 10$ pN which have been

measured for PfEMP1–CD36 bond.[48] We used on-rate $\kappa_{on} = 8$ Hz. We have also checked that variation of on-rate changes tracking lengths, but it does not change the nature of the results.
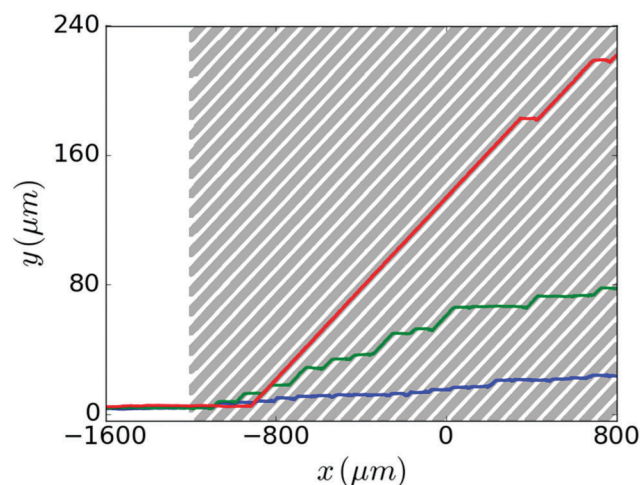

Fig. 6 Adhesive dynamics simulations of malaria-infected red blood cells. Representative trajectories are shown for rings (blue), trophozoite (green) and schizont (red) stage cells on ligand patterns with an inclination angle $\alpha = 8°$ and at shear rate $\dot{\gamma} = 30$ Hz.
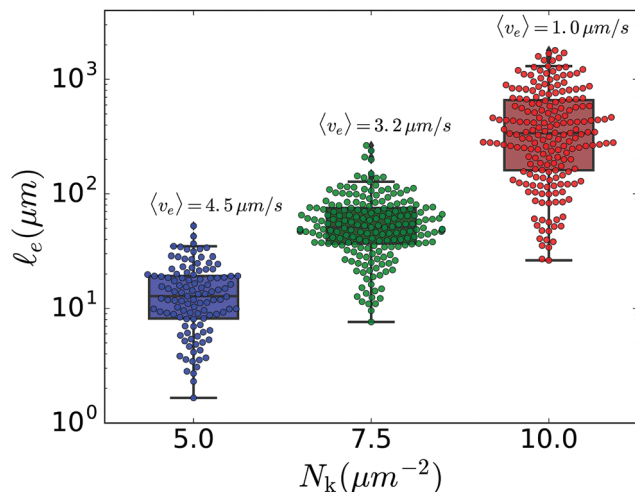
Fig. 7 Mean tracking lengths for the three stages of infectious cells are shown. Average velocities are also displayed at the top of respective data points.

In Fig. 6, we show representative trajectories for rings, trophozoites and schizonts. The ring stage trajectory, having very small tracking lengths, has the lowest lateral displacement. The trophozoite, having moderate knob density, ends up at about 80 μm of lateral displacement. The schizont with higher knob density ends up at the top of grid close to 220 μm. These representative trajectories show that the three types of cells will

end up at different locations for realistic parameter choices. In Fig. 7, we plot the edge tracking lengths for these three types of cells. In addition we display the average velocities on top of corresponding data points. Ring cells have higher velocity of 4.5 μm s^{-1} and mean tracking length of 15 μm, while schizonts have lower velocity of 1.0 μm s^{-1} and mean tracking length of 462 μm. We see that it is important that all three types of cells have distinct range of tracking lengths so that they end up at different lateral positions.

In Fig. 8(A), we show the distributions of the total lateral displacements of the three cell types at the end of the grid shown in Fig. 6 (length 2 mm) for $\alpha = 8°$. For comparison, in Fig. 8(B) and (C), we show the same total lateral displacements for edge inclination angles $\alpha = 6°$ and $\alpha = 10°$. The three stages of infected cells end up at different locations at the end of the grid which means that these three types of cells can be sorted from mixed populations. The total lateral displacements for the ring stage cells is small and its distribution is close to zero, where other non-adhesive cells from heterogeneous blood cell populations aggregate. From the plots, it is also clear that the distributions of three stages of infected cells are better isolated for $\alpha = 8°$ than for smaller or higher angles. The separation between these populations can be increased by increasing the number of stripes.

To better understand these observations, we have applied an optimal angle analysis to these three types of cells. In Fig. 8(D), we show the total lateral displacement L_d from eqn (6) for these
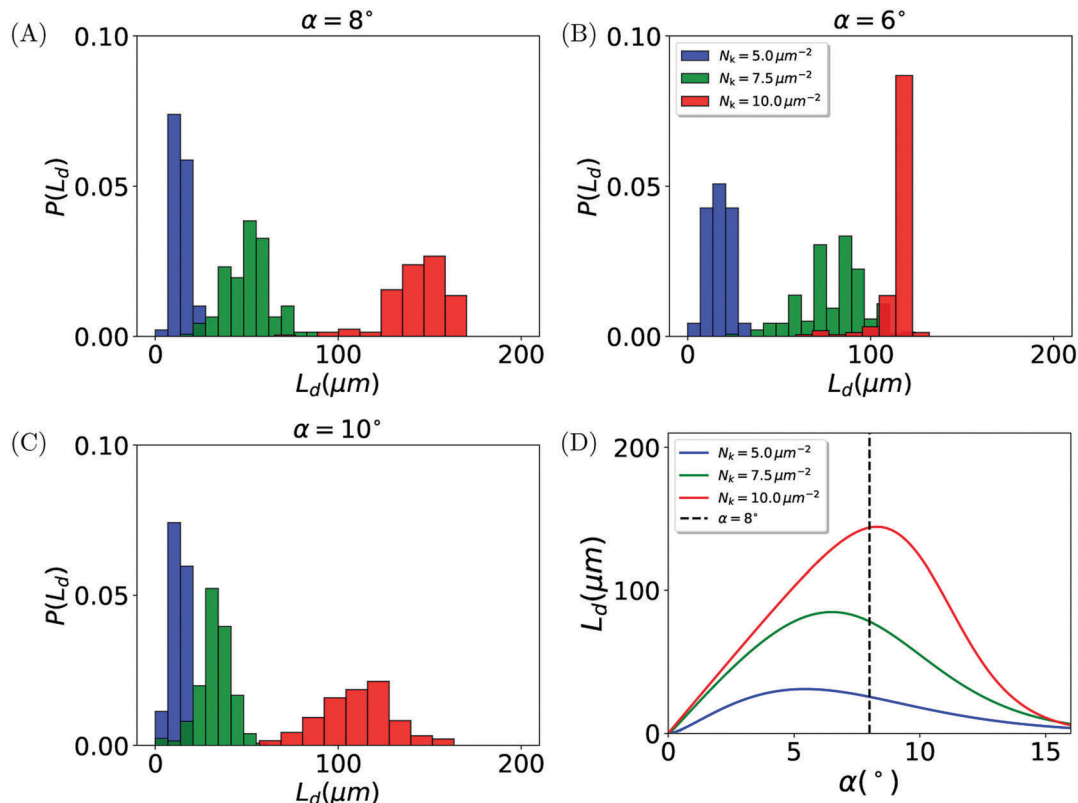

Fig. 8 Distributions of total lateral displacements of rings (blue color), trophozoites (green color) and schizonts (red color) are shown for edge inclination angles (A) $\alpha = 8°$, (B) $\alpha = 6°$ and (C) $\alpha = 10°$. (D) Total lateral displacements L_d computed using eqn (6) for rings, trophozoites and schizonts.

three cell types. The optimal angle at which L_d is maximum increased with the knob density, resulting in a higher angle for schizonts and smaller angle for rings. The optimal angle for schizont cells is close to $8°$, which is shown as dotted line. Let's say α_{RT} is the angle at which the difference between total lateral displacements of rings and trophozoites $|L_d^R - L_d^T|$ is maximum. Similarly α_{TS} is the angle at which the difference between total lateral displacements of trophozoites and schizonts $|L_d^T - L_d^S|$ is maximum and α_R is the angle at which L_d^R is maximum. These critical angles α_R, α_{RT} and α_{TS} are found to be close to $5°$, $7°$ and $9°$, respectively. Now the optimum angle for sorting all three types of cells should be such that the product of differences ($|L_d^R| \times |L_d^R - L_d^T| \times |L_d^T - L_d^S|$) is maximum, which essentially ensures good sorting efficiency. This optimum angle is found to be $\simeq 7.8°$, which is close to what we chose. Thus our choice $\alpha = 8°$ is a reasonably good choice for sorting the three types of iRBCs.

4 Conclusions

In this article, we studied the rolling adhesion of leukocytes and malaria-infected red blood cells on ligand patterned stripe assays in shear flow. Surprisingly, both systems share a lot of common features.[26] We have used a rigid spherical cell of radius $R = 4$ μm and covered it with adhesive patches containing several receptors. We have used mean value of 6 receptors for each patch (distributed with Poisson distribution) which has been estimated indirectly for iRBCs.[48] We first have compared our simulation results with the experimental results on sorting of leukocytes from whole blood on P-selectin (which binds to PSGL receptor on leukocytes) patterned assays.[16] We have discussed the effect of key parameters such as inclination angle or shear rate on edge tracking lengths and we have shown that for a fixed grid there exists an optimal angle at which total lateral displacement is maximum. Using our simulations, we have also shown that the adhesive footprint becomes smaller and asymmetric for increasing inclination angle. Decreasing the contact area with increasing inclination angle makes the motion transient and faster. Finally, we have shown using simulations that the three main stages of malaria-infected blood cells can be sorted and we have identified relevant parameters for experiments, such as inclination angle and shear rate.

The main deficiency of our study in terms of sorting iRBCs is the fact that we have distinguished between the three infectious stages only by their knob densities, although it is well known that they also have different shapes and mechanics.[53] While schizont stage cells are rigid and close to spherical shape as assumed here, ring and trophozoite cells have asymmetric discoid shape and they are more deformable compared to schizonts.[54] We have also shown earlier that because of asymmetric discoid shape and its deformability, trophozoites flip rather than roll, whereas schizonts roll.[35] In this work, we limited ourselves to account only for knob differences in these cells rather than shape or deformability, in order to be able to analyze this interesting system with good statistics. However, in

preliminary work, we implemented a deformable cell model with multi-particle collision dynamics (MPCD) solvent and we found that the same sorting effect persists and even becomes stronger in a deformable cell model (Dasanna and Schwarz, unpublished). The main effect here is that trophozoites start to flip, which makes their edge-tracking motion even more unstable, thus schizonts show even larger lateral displacement. Adhesive dynamics as used here have the essential advantage that they allow us to achieve good statistics with moderate computational effort, which in turn is very helpful for rational design as suggested here. We expect that in the future, such rational design of adhesion-based cell sorting devices will be very useful for a large range of applications in medicine and biotechnology.

Conflicts of interest

There are no conflicts to declare.

Acknowledgements

Notes and references

1 P. Sajeesh and A. K. Sen, *Microfluid. Nanofluid.*, 2014, **17**, 1–52.

2 T. M. Geislinger and T. Franke, *Adv. Colloid Interface Sci.*, 2014, **208**, 161–176.

3 C. W. Shields IV, C. D. Reyes and G. P. López, *Lab Chip*, 2015, **15**, 1230–1249.

4 M. Yamada, M. Nakashima and M. Seki, *Anal. Chem.*, 2004, **76**, 5465–5471.

5 T. Morijiri, S. Sunahiro, M. Senaha, M. Yamada and M. Seki, *Microfluid. Nanofluid.*, 2011, **11**, 105–110.

6 J.-S. Park and H.-I. Jung, *Anal. Chem.*, 2009, **81**, 8280–8288.

7 L. R. Huang, E. C. Cox, R. H. Austin and J. C. Sturm, *Science*, 2004, **304**, 987–990.

8 J. McGrath, M. Jimenez and H. Bridle, *Lab Chip*, 2014, **14**, 4139–4158.

9 J. P. Beech, S. H. Holm, K. Adolfsson and J. O. Tegenfeldt, *Lab Chip*, 2012, **12**, 1048–1051.

10 D. Holmes, G. Whyte, J. Bailey, N. Vergara-Irigaray, A. Ekpenyong, J. Guck and T. Duke, *Interface Focus*, 2014, **4**, 20140011.

11 E. Henry, S. H. Holm, Z. Zhang, J. P. Beech, J. O. Tegenfeldt, D. A. Fedosov and G. Gompper, *Sci. Rep.*, 2016, **6**, 34375.

12 O. Otto, P. Rosendahl, A. Mietke, S. Golfier, C. Herold, D. Klaue, S. Girardo, S. Pagliara, A. Ekpenyong and A. Jacobi, *et al.*, *Nat. Methods*, 2015, **12**, 199–202.

13 M. Xavier, P. Rosendahl, M. Herbig, M. Kräter, D. Spencer, M. Bornhäuser, R. O. Oreffo, H. Morgan, J. Guck and O. Otto, *Integr. Biol.*, 2016, **8**, 616–623.

14 M. B. Lawrence and T. A. Springer, *Cell*, 1991, **65**, 859–873.

15 R. P. McEver and C. Zhu, *Annu. Rev. Cell Dev. Biol.*, 2010, **26**, 363.

16 C.-H. Lee, S. Bose, K. J. V. Vliet, J. M. Karp and R. Karnik, *Langmuir*, 2011, **27**, 240–249.

17 S. Bose, R. Singh, M. Hanewich-Hollatz, C. Shen, C.-H. Lee, D. M. Dorfman, J. M. Karp and R. Karnik, *Sci. Rep.*, 2013, **3**, 2329.

18 S. Choi, J. M. Karp and R. Karnik, *Lab Chip*, 2012, **12**, 1427–1430.

19 A. Hochstetter and T. Pfohl, *Trends Parasitol.*, 2016, **32**, 531–541.

20 S. H. Holm, J. P. Beech, M. P. Barrett and J. O. Tegenfeldt, *Lab Chip*, 2011, **11**, 1326–1332.

21 S. Suresh, J. Spatz, J. Mills, A. Micoulet, M. Dao, C. Lim, M. Beil and T. Seufferlein, *Acta Biomater.*, 2005, **1**, 15–30.

22 H. W. Hou, A. A. S. Bhagat, A. G. L. Chong, P. Mao, K. S. W. Tan, J. Han and C. T. Lim, *Lab Chip*, 2010, **10**, 2605–2613.

23 T. M. Geislinger, S. Chan, K. Moll, A. Wixforth, M. Wahlgren and T. Franke, *Malar. J.*, 2014, **13**, 375.

24 N. Toepfner, C. Herold, O. Otto, P. Rosendahl, A. Jacobi, M. Kräter, J. Stächele, L. Menschner, M. Herbig and L. Ciuffreda, *et al.*, *eLife*, 2018, **7**, e29213.

25 L. H. Miller, D. I. Baruch, K. Marsh and O. K. Doumbo, *Nature*, 2002, **415**, 673–679.

26 G. Helms, A. K. Dasanna, U. S. Schwarz and M. Lanzer, *FEBS Lett.*, 2016, **590**, 1955–1971.

27 D. Hammer and S. Apte, *Biophys. J.*, 1992, **63**, 35–57.

28 D. A. Hammer, *J. Biomech. Eng.*, 2014, **136**, 021006.

29 C. Korn and U. Schwarz, *Phys. Rev. Lett.*, 2006, **97**, 138103.

30 C. B. Korn and U. S. Schwarz, *Phys. Rev. E: Stat., Nonlinear, Soft Matter Phys.*, 2008, **77**, 041904.

31 X. Zheng, L. S.-L. Cheung, J. A. Schroeder, L. Jiang and Y. Zohar, *Lab Chip*, 2011, **11**, 3431–3439.

32 K. Ramesh, R. Thaokar, J. R. Prakash and R. Prabhakar, *Phys. Rev. E: Stat., Nonlinear, Soft Matter Phys.*, 2015, **91**, 022302.

33 S. Jadhav, C. D. Eggleton and K. Konstantopoulos, *Biophys. J.*, 2005, **88**, 96–104.

34 Z. Y. Luo and B. F. Bai, *Soft Matter*, 2016, **12**, 6918–6925.

35 A. K. Dasanna, C. Lansche, M. Lanzer and U. S. Schwarz, *Biophys. J.*, 2017, **112**, 1908–1919.

36 D. A. Fedosov, B. Caswell, S. Suresh and G. E. Karniadakis, *Proc. Natl. Acad. Sci. U. S. A.*, 2011, **108**, 35–39.

37 D. A. Fedosov, B. Caswell and G. E. Karniadakis, *Biophys. J.*, 2011, **100**, 2084–2093.

38 C. B. Korn and U. S. Schwarz, *J. Chem. Phys.*, 2007, **126**, 9.

39 G. Bell, *Cell Biochem. Biophys.*, 1981, **3**, 289–304.

40 C. B. Korn, S. Klumpp, R. Lipowsky and U. S. Schwarz, *J. Chem. Phys.*, 2009, **131**, 12B624.

41 K. D. Patel, M. U. Nollert and R. P. McEver, *J. Cell Biol.*, 1995, **131**, 1893–1902.

42 M. Rug, S. W. Prescott, K. M. Fernandez, B. M. Cooke and A. F. Cowman, *Blood*, 2006, **108**, 370–378.

43 R. R. Akhouri, S. Goel, H. Furusho, U. Skoglund and M. Wahlgren, *Cell Rep.*, 2016, **14**, 723–736.

44 B. T. Marshall, M. Long, J. W. Piper, T. Yago, R. P. McEver and C. Zhu, *Nature*, 2003, **423**, 190–193.

45 W. Hanley, O. McCarty, S. Jadhav, Y. Tseng, D. Wirtz and K. Konstantopoulos, *J. Biol. Chem.*, 2003, **278**, 10556–10561.

46 W. D. Hanley, D. Wirtz and K. Konstantopoulos, *J. Cell Sci.*, 2004, **117**, 2503–2511.

47 V. Heinrich, A. Leung and E. Evans, *Biophys. J.*, 2005, **88**, 2299–2308.

48 X. Xu, A. K. Efremov, A. Li, L. Lai, M. Dao, C. T. Lim and J. Cao, *PLoS One*, 2013, **8**, e64763.

49 J.-Y. Shao, H. P. Ting-Beall and R. M. Hochmuth, *Proc. Natl. Acad. Sci. U. S. A.*, 1998, **95**, 6797–6802.

50 S. Majstoravich, J. Zhang, S. Nicholson-Dykstra, S. Linder, W. Friedrich, K. A. Siminovitch and H. N. Higgs, *Blood*, 2004, **104**, 1396–1403.

51 E. Evans, V. Heinrich, A. Leung and K. Kinoshita, *Biophys. J.*, 2005, **88**, 2288–2298.

52 H. Rieger, H. Y. Yoshikawa, K. Quadt, M. A. Nielsen, C. P. Sanchez, A. Salanti, M. Tanaka and M. Lanzer, *Blood*, 2015, **125**, 383–391.

53 A. K. Dasanna, U. S. Schwarz, G. Gompper and D. A. Fedosov, in *Multiscale Modeling of Malaria-Infected Red Blood Cells*, ed. W. Andreoni and S. Yip, Springer International Publishing, Cham, 2018, pp. 1–24.

54 M. Waldecker, A. K. Dasanna, C. Lansche, M. Linke, S. Srismith, M. Cyrklaff, C. Sanchez, U. Schwarz and M. Lanzer, *Cell. Microbiol.*, 2017, **19**(2), e12650.